Extreme star formation events in quasar hosts over $0.5 < z < 4$

L. K. Pitchford,[1,2]* E. Hatziminaoglou,[1] A. Feltre,[3] D. Farrah,[2] C. Clarke,[4] K. A. Harris,[2,5] P. Hurley,[4] S. Oliver,[4] M. Page[6] and L. Wang[7]

[1]*ESO, Karl-Schwarzschild-Str. 2, D-85748 Garching bei München, Germany*
[2]*Department of Physics, Virginia Tech, Blacksburg, VA 24061, USA*
[3]*Sorbonne universités, UPMC-CNRS, UMR7095, Institut d'Astrophysique de Paris, F-75014 Paris, France*
[4]*Astronomy Centre, Department of Physics and Astronomy, University of Sussex, Brighton BN1 9QH, UK*
[5]*Instituto de Astrofísica de Canarias, C/via Láctea s/n, E-38205 La Laguna, Tenerife, Spain*
[6]*Mullard Space Science Laboratory, University College London, Holmbury St Mary, Dorking, Surrey RH5 6NT, UK*
[7]*SRON Netherlands Institute for Space Research, Landleven 12, NL-9747 AD, Groningen, the Netherlands*

ABSTRACT

We explore the relationship between active galactic nuclei (AGN) and star formation in a sample of 513 optically luminous type 1 quasars up to redshifts of ~4 hosting extremely high star formation rates (SFRs). The quasars are selected to be individually detected by the *Herschel* SPIRE instrument at $>3\sigma$ at 250 μm, leading to typical SFRs of order of 1000 $M_\odot$ yr^{-1}. We find the average SFRs to increase by almost a factor 10 from $z \sim 0.5$ to $z \sim 3$, mirroring the rise in the comoving SFR density over the same epoch. However, we find that the SFRs remain approximately constant with increasing accretion luminosity for accretion luminosities above 10^{12} L$_\odot$. We also find that the SFRs do not correlate with black hole mass. Both of these results are most plausibly explained by the existence of a self-regulation process by the starburst at high SFRs, which controls SFRs on time-scales comparable to or shorter than the AGN or starburst duty cycles. We additionally find that SFRs do not depend on Eddington ratio at any redshift, consistent with no relation between SFR and black hole growth rate per unit black hole mass. Finally, we find that high-ionization broad absorption line (HiBAL) quasars have indistinguishable far-infrared properties to those of classical quasars, consistent with HiBAL quasars being normal quasars observed along a particular line of sight, with the outflows in HiBAL quasars not having any measurable effect on the star formation in their hosts.

Key words: quasars: general – galaxies: starburst – galaxies: star formation – infrared: galaxies.

1 INTRODUCTION

Nuclear activity and star formation in galaxies are observed to often coexist across all redshifts (Farrah et al. 2003; Alexander et al. 2005; Hernán-Caballero et al. 2009; Shi et al. 2009; Hatziminaoglou et al. 2010; Mainieri et al. 2011; LaMassa et al. 2013; Alaghband-Zadeh et al. 2016; Harris et al. 2016), up to extremely high active galactic nuclei (AGN) and starburst luminosities (e.g. Genzel et al. 1998; Carilli et al. 2001; Omont et al. 2001; Farrah et al. 2002; Efstathiou et al. 2014; Magdis et al. 2014; Rosenberg et al. 2015). Moreover, there is a tight correlation between the stellar velocity dispersion in the bulge and the mass of the supermassive black hole (BH) residing in the centre for nearby quiescent galaxies (e.g. Magorrian et al. 1998; Ferrarese & Merritt 2000; Tremaine et al. 2002; Häring & Rix 2004). These observations suggest that there exists a deep connection between stellar and BH mass assembly events in galaxies.

The nature of, and connection between, star formation and AGN activity in galaxies is unclear. For starbursts, the majority of star-forming systems lie on a 'main sequence' whose mean star formation rate (SFR) rises with redshift, from about 10 $M_\odot$ yr^{-1} at $z = 0.5$ to roughly 100 $M_\odot$ yr^{-1} at $z = 2$ (as in e.g. Elbaz et al. 2011; Rodighiero et al. 2011; Schreiber et al. 2015). The origin of this main sequence is however still debated, as is the trigger for star formation as a function of a galaxy's position relative to the main sequence. For AGN, it is difficult to complete a robust census of AGN from surveys, since they are obscured by dust and gas for a significant fraction of their lives, with this fraction possibly dependent upon both luminosity and redshift (e.g. Martínez-Sansigre et al. 2005). It is also unclear if star formation events and AGN activity can directly affect one another. A direct relation is motivated by models

for galaxy assembly to improve consistency between predictions and observations, most often via 'quenching' of star formation by an AGN (e.g. Bower et al. 2006; Croton et al. 2006; Booth & Schaye 2009; Fabian 2012). However, observational studies of quenching remain inconclusive. Indirect manifestations of feedback, such as large molecular gas outflows (e.g. Feruglio et al. 2010; Spoon et al. 2013) and powerful AGN-driven winds (e.g. Perna et al. 2015), are found routinely (see also e.g. Farrah et al. 2009; Bridge et al. 2013; Spoon et al. 2013), but studies that claim a causal relation are rarer (Farrah et al. 2012; Page et al. 2012), and sometimes controversial (e.g. Harrison et al. 2014).

As a result, the scaling relations between star formation and AGN activity across their respective duty cycles remain uncertain. Some authors find a scaling between SFR and AGN luminosity (e.g. Imanishi et al. 2011; Young et al. 2014; Delvecchio et al. 2015), while others do not (e.g. Shao et al. 2010; Mullaney et al. 2012b; Harrison et al. 2014; Ma & Yan 2015; Stanley et al. 2015). Recently, Harris et al. (2016) have shown that a correlation between SFR and AGN luminosity may only exist over certain AGN luminosity, SFR and redshift ranges.

An insightful way to study the connections between star formation and AGN activity in the context of galaxy assembly events is to examine their scaling relations in populations that signpost specific regions of the AGN luminosity and SFR parameter space. One such population are optically luminous type 1 quasars that host luminous, off-main sequence starbursts. This population is straightforward to find in optical surveys, corresponds to a specific phase in the AGN duty cycle, and may signpost the extremes of the starburst duty cycle. As such, they may illustrate how the processes that convert free baryons to stellar and BH mass may change at the most extreme luminosities. They are also an excellent population in which to search for the initial stages of AGN feedback.

A related population within which it would appear intuitive to search for evidence of AGN feedback is that of the broad absorption line (BAL) quasars (Lynds 1967; Turnshek 1984). The BAL quasars possess broad P-Cygni-like absorption features in their ultraviolet spectra that are blue-shifted with respect to the nominal wavelength of the emission line. These features may stem from outflows from the quasars and may further be associated with high mass-loss rates (de Kool et al. 2002; Chartas, Brandt & Gallagher 2003). These outflows could arise in two ways; the outflows could be a random process, present for only a random fraction of the quasar lifetime and/or over certain viewing angles (e.g. Elvis 2000). The observation of BALs in only 10–15 per cent of quasars (e.g. Hewett & Foltz 2003) then arises from a suitable combination of these two factors. Secondly, BALs may signpost outflows that occur only at a particular point in a quasar's lifetime, most likely 'young' objects recently (re)fuelled by mergers that also trigger star formation in their hosts. It is this second scenario that would mean that BAL quasars may signpost quasar-mode feedback. This may manifest itself via BAL quasars having different far-infrared (FIR) properties, on average, to those of ordinary quasars.

In this paper, we undertake such a study, exploring the relationship between star formation and AGN activity in optically luminous quasars over $0.5 < z < 4$ that host extremely high SFRs, from 40 to 4000 $M_\odot$ yr^{-1}, placing these hosts approximately one dex above the star formation main sequence. To do so, we start with quasars in the Sloan Digital Sky Survey (SDSS) in Data Releases 7 and 10 (DR7 and DR10, respectively) that also lie within extragalactic survey fields covered by the Spectral and Photometric Imaging Receiver (SPIRE; Griffin et al. 2010) instrument onboard *Herschel* (Pilbratt et al. 2010). We then restrict ourselves to those quasars

that are individually detected by *Herschel*. We infer SFRs from the *Herschel* data, and compare these to the properties of the AGN, as measured from the SDSS catalogue data. We also examine the properties of BAL quasars to see if their properties show evidence for AGN feedback.

The paper is structured as follows. The SDSS and *Herschel* data, as well as the matched quasar catalogue, are described in Section 2. Further, Section 3 describes the spectral energy distribution (SED) fitting, the SFR derivation and uncertainties and discusses the way in which the current study complements previous works in terms of samples and methodology. Section 4 presents the SFRs in the full quasar sample and in the BAL quasar sub-sample separately, as a function of the quasars' intrinsic properties, namely accretion luminosity, BH mass and Eddington ratio. Lastly, Section 5 discusses our results and places them in a greater context. Throughout this work, we assume $H_0 = 72$ km s^{-1} Mpc^{-1}, $\Omega_\Lambda = 0.7$ and $\Omega_M = 0.3$.

2 DATA

2.1 SDSS data

We assemble our parent quasar sample from a combination of the SDSS quasar catalogues from DR7 (Schneider et al. 2010) and DR10 (Pâris et al. 2014). The location within the SDSS colour-space provides the basis for the selection of most quasar candidates, with Richards et al. (2002) describing the original SDSS selection criteria. For an object with an ultraviolet excess (typical for quasars) to be selected for spectroscopic follow-up, it should be brighter than $i \sim 19.1$ ($i \sim 20.2$) if its estimated redshift based on its colours is $z \lesssim 3$ ($z \gtrsim 3$). However, the quasar candidate selection criteria applied through DR7 were biasing the selection against objects with $z \gtrsim 2.2$. The Baryon Oscillation Spectroscopic Survey (BOSS) quasars included in DR10, on the other hand, were sought for in the redshift range between 2.15 and 3.5, down to fainter magnitudes ($g < 22.0$ or $r < 21.85$), in order to reach a higher quasar surface density (Ross et al. 2012). We include both DR7 and DR10 quasars to get a larger and more uniform redshift coverage. Had we opted for DR7 (DR10) alone, we would have missed the bulk of the $z > 2$ ($z < 2$) quasars. The resulting combined sample, though not complete in redshift, covers a more representative space in absolute i-band magnitude, M_i, and redshift than would either of the two data releases individually.

As a function of redshift, DR7 is more than 90 per cent complete up to redshifts of about 2.2 (Richards et al. 2002). Thus, DR10 was designed to target objects above this redshift; that is, quasars at $2.15 \leq z \leq 3.5$, over which the CORE selection is homogeneous and uniform (Ross et al. 2012; White et al. 2012). Within this range, DR10 has a given maximum completeness from single-epoch data of 70 per cent at $z = 2.2$ (Ross et al. 2012, fig. 14). As such, some of the highest redshift BAL quasars might be missing from our sample.

The combined use of DR7 and DR10, without any restrictions, potentially affects the overall completeness and uniformity of the sample, since the different apparent magnitude cuts in the two releases could make the combined sample incomplete in terms of redshift. K–S tests on the distribution of the various colours and M_i however yield p-values (all above 0.4) that cannot reject the null hypothesis that the DR7 and DR10 sub-samples come from the same colour and M_i parent distributions. Moreover, Ma & Yan (2015), who also study the FIR properties of a combined sample of quasars from DR7 and DR10, similarly reach the conclusion that any incompleteness resulting from the non-uniform selection of targets in the two releases does not affect the validity of such a study.

Table 1. Quasar detection statistics by survey. The overlapping region is the area of each *Herschel* field that is also covered by SDSS. The SDSS detections are those quasars that lie in their respective *Herschel* fields. The joint detections columns represent those SDSS quasars with SPIRE detections above 3σ at 250 μm. We further describe these objects by the data release in which they are found: DR7 or DR10. The sum of the DR7 and DR10 columns is always higher than the columns showing the totals, as the latter only consider unique entries. The SDSS detections columns represent those SDSS quasars located in each respective *Herschel* field, while the joint detections are the quasars with 250 μm detections at $>3\sigma$.

Field	Overlapping Region (deg^2)	SDSS quasars			*Herschel*/SDSS quasars		
		Total	In DR7	In DR10	Total	In DR7	In DR10
HerMES	60	1293	586	739	83	43	44
HerS	79	4524	2154	2779	212	150	90
HeLMS	210	8827	2488	6796	218	92	144

2.2 *Herschel* data

We look for *Herschel* counterparts to our SDSS quasar sample in the *Herschel* Multi-tiered Extragalactic Survey (HerMES; Oliver et al. 2012) and the *Herschel* Stripe 82 Survey (HerS; Viero et al. 2014). HerS consists of 79 deg^2 of contiguous SPIRE imaging of the SDSS 'Stripe 82'. The HerMES fields considered here are the HerMES Large Mode Survey (HeLMS) field, the widest HerMES tier spanning 270 deg^2 observed with SPIRE alone, as well as the northern Level 5 and 6 fields of Bootes, EGS, ELAIS-N1, Lockman, FLS and *XMM*-LSS, selected for their overlap with the SDSS footprint. The total area we select is thus ~350 deg^2.

The point source catalogues from which we extract the SPIRE fluxes in the smaller HerMES fields are presented in Wang et al. (2014). The HeLMS catalogue is part of the HerMES DR4 and is also briefly discussed in Wang et al. (2015). The HeLMS SPIRE maps are also part of the HerMES DR3. Here we give a summary of the point source catalogue creation, as well as its completeness, accuracy and reliability. For a full description, see Clarke (2016).[1] The HeLMS point source catalogue was created using the HerMES pipeline, a combination of the STARFINDER and DESPHOT algorithms. STARFINDER (Diolaiti et al. 2000) is an iterative source-finding algorithm initially developed for crowded stellar fields. As such, STARFINDER can de-blend confused *Herschel* sources to find positions, but it requires the background to be mostly free from source flux. In *Herschel* SPIRE maps, however, the sky is comprised almost entirely of flux from sources. As such, STARFINDER does not accurately estimate fluxes. Thus, DESPHOT (De-blended SPIRE Photometry algorithm; Roseboom et al. 2010, 2012) is used instead, with the STARFINDER objects as positional priors.

Both the HeLMS and HerS fields are contaminated by Galactic cirrus. This is in contrast to the other HerMES fields on which the source extraction techniques were developed, which are relatively free from cirrus; thus, both the maps and the source extraction techniques have to be modified. FIR emission from cirrus boosts fluxes of sources behind it such that a naive source extraction will find more and brighter sources in a cirrus-contaminated region. Cirrus has structure on large scales, as opposed to the small-scale fluctuations in the map from extragalactic sources, so emission from cirrus can be removed using a high-pass filter. For consistency, we adopt the filtering technique applied for HerS, as defined in Viero et al. (2014), for the creation of the HeLMS catalogue.

The confusion noise and background have been calculated from the entire map rather than on individual tiles, into which the large map has been segmented at the time of source extraction (for details

see Viero et al. 2014). The total error on each source is given as $\sigma_{\rm T} = \sqrt{\sigma_{\rm conf}^2 + \sigma_{\rm inst}^2}$, with $\sigma_{\rm inst}^2$ as the instrumental noise. The confusion noise, $\sigma_{\rm conf}^2$, has been calculated on the residual map by fitting a line to the flux as a function of coverage, where the confusion noise is the *y*-intercept. Any source with $\chi^2 > 10$ is removed from the catalogue, leaving a total of 92 256 sources at 250 μm.

To test the positional and flux accuracy, we inject sources of known fluxes at random positions in the map. The maps are then run through the source extraction pipeline again. We find the positional accuracy to be within 5 arcsec in both right ascension and declination. The flux accuracy is already above 90 per cent at 30 mJy and reaches 98 per cent at 40 mJy.

Finally, to match the catalogues in the three SPIRE bands and assess completeness, we follow Smith et al. (2012). We find a maximum completeness of 93 per cent, attained at ~60 mJy. The remaining sources are missed by the STARFINDER algorithm, but are not associated with any particular region of the map (see also Wang et al. 2014).

2.3 SDSS–*Herschel* matching

Wang et al. (2014) have shown through simulations, in the fashion mentioned above, that the positional accuracy of sources in the DR2 HerMES point source catalogues also peaks at 5 arcsec. We therefore look for SDSS DR7 and DR10 quasars with $>3\sigma$ detections at 250 μm applied across all the fields, using a 5 arcsec matching radius between the SDSS and *Herschel* catalogues. The results of this match are provided in Table 1. Note that we rely on the individually detected objects only and do not stack the SPIRE fluxes of the non-detected SDSS quasars. Our final catalogue contains 83, 212 and 218 unique SDSS quasars (i.e. they only appear once in the catalogue even if they belong to both DR7 and DR10) in the HerMES fields, HerS and HeLMS, respectively. In what follows, we call these 513 quasars the *Herschel*/SDSS quasar sample.

The *Herschel*/SDSS quasars span the redshift range $0.1627 \leq z \leq 4.679$, and the bulk lie in the M_i (as defined in Schneider et al. 2010) range between -22.5 and -29. The $M_i - z$ plane of the sample is shown in Fig. 1, where the DR7 and DR10 objects are marked in red circles and blue squares, respectively. The filled symbols denote BAL quasars and will be discussed separately. The histograms of the quasars belonging to the DR7 and DR10 releases, as well as that of the final sample, are shown in the top figure as filled red bars, dashed blue and solid black lines, respectively. The green spikes show the redshift distribution of the BAL quasars.

The 350 and 500 μm fluxes are extracted on the 250 μm positions, but we apply no cuts in signal to noise for either the 350 or the 500 μm fluxes. This results in 505 detections at 350 μm

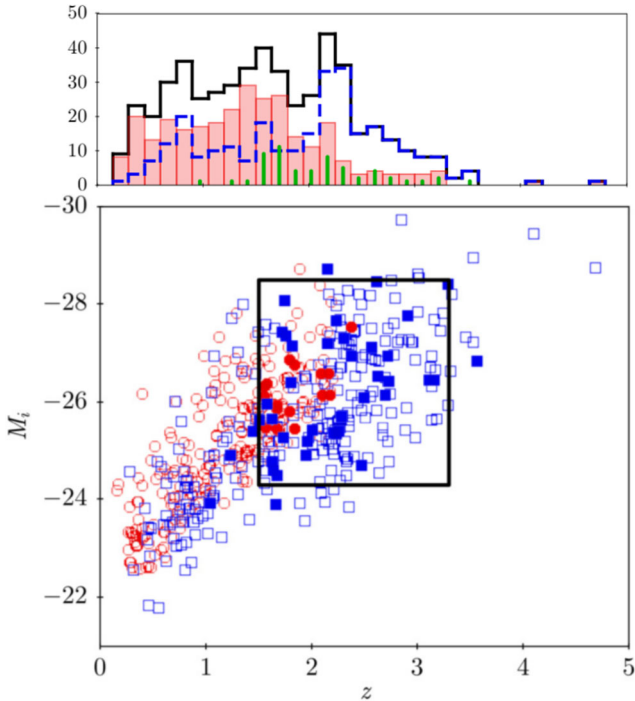[1] Doctoral thesis, available through Sussex Research Online: http://sro.sussex.ac.uk/61474/.

Figure 1. Absolute *i*-band magnitude versus redshift. The red circles represent those objects included in SDSS DR7, while the blue squares are those objects in DR10. The filled and open shapes differentiate between the BAL and non-BAL samples, respectively (see Section 4.2). To characterize these BAL and non-BAL subsets we use the objects that lie within the black box, with its limits defined by $1.5 \leq z \leq 3.3$ and $-28.5 \leq M_i \leq -24.3$, in which most of the BAL quasars lie. The redshift histograms are shown at the top, with the filled red, dashed blue and solid black showing the DR7, DR10 and full sample of objects, respectively. The green spikes represent the redshift distribution of the BAL quasars.
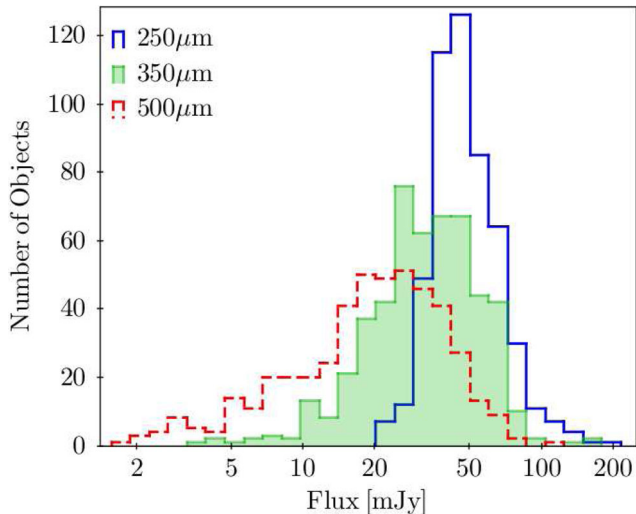

Figure 2. SPIRE flux distributions of the *Herschel*/SDSS quasar sample. In the solid blue, filled green and dashed red histograms, we show the 250 μm, 350 μm and 500 μm fluxes, respectively.

and 473 detections at 500 μm. The SPIRE flux distributions of the *Herschel*/SDSS quasar sample are shown in Fig. 2.

The *Herschel* detection rates at 250 μm of SDSS quasars in our fields average at ∼5 per cent, as seen when comparing the 3rd and 6th columns of Table 1, with a constant detection fraction up

to $M_i \sim -27$ and an increase by a factor of ∼1.5 towards brighter absolute magnitudes. This number is smaller than the detection rates mentioned in previous works (e.g. Hatziminaoglou et al. 2010, who find a 30 per cent detection rate in Lockman and FLS at 5σ but for both type 1 and type 2 AGN combined). The lower detection rates within our sample are largely due to the fact that HerS and HeLMS, where 85 per cent our quasars are located, are shallower than the HerMES fields. Our detection rates are instead more in line with the 8 per cent detection rate presented in Bonfield et al. (2011), using a simple positional cross-match in the H-ATLAS science demonstration field.

2.4 Ancillary data

Of our 513 quasars, 473 are also detected by the Wide-Field Infrared Survey Explorer (WISE; Wright et al. 2010). We also assemble near-infrared detections from three surveys: the Two Micron All Sky Survey (2MASS; Skrutskie et al. 2006), the UKIRT Infrared Deep Sky Survey (UKIDSS; Lawrence et al. 2007), and the VISTA Hemisphere Survey (VHS; McMahon et al. 2013) Data Release 3. There are 196 objects in the HerS catalogue with a measurement in one or more of the UKIDSS bands and 178 within HeLMS. There are also 64 objects (16, 14 and 34 in HerMES, HerS and HeLMS, respectively) with VHS photometry. Finally, 29 objects have a measurement in at least one of the 2MASS bands. While HerS and HeLMS also have 2MASS data available, we choose to use the UKIDSS data, as it is deeper. As a result, for more than 90 per cent of our objects, there is a minimum of 11 and a maximum of 16 photometric data points available from the optical to the FIR.

3 ANALYSIS

3.1 Starburst and AGN luminosities

To infer starburst and AGN luminosities, we use the multicomponent SED fitting technique described in Hatziminaoglou et al. (2008) and Hatziminaoglou, Fritz & Jarrett (2009). In the most general case, the method fits fluxes and their errors with three separate models: stellar, AGN, and starburst. Our sample however consists entirely of luminous type 1 quasars with extremely high SFRs. This allows us to make two key simplifications to the general method. First, it is almost certain that the stellar emission will be outshone by the AGN and/or the starburst at all wavelengths, so we do not include a stellar template in the fit. Second, since our sources are type 1 quasars, it is reasonable to conclude that the optical to mid-infrared (MIR) coverage will be dominated by the AGN (Hatziminaoglou et al. 2005), and that the FIR coverage will be dominated by the starburst (e.g. Hatziminaoglou et al. 2010; Ma & Yan 2015; Harris et al. 2016). The infrared emission reprocessed by the AGN torus strongly depends on the dust geometry. In particular, the ratio between the outer and inner radius of the torus plays a major role in determining the AGN SED at longer wavelengths (in the models used in this paper the maximum value of this ratio is 150). As a result, the peak of the infrared emission of the AGN torus models lies at 10–30 μm (fig. 5 of Feltre et al. 2012) and the maximum width of the infrared bump (as defined in Feltre et al. 2012) for these models is ∼50 μm. We therefore do not expect any significant contribution from the AGN emission at wavelengths larger than ∼50 μm. Complementary, observationally motivated discussion on this point can be found in section 5.3 of Harris et al. (2016). We note the caveat though that, with our data, which do not cover the range between 22 and 250 μm, we cannot completely rule out significant
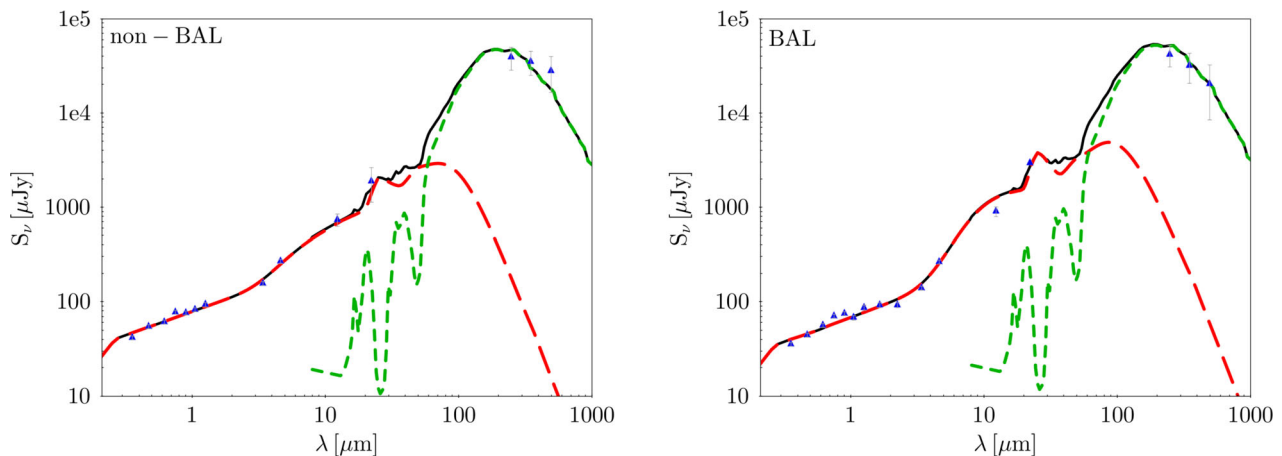
Figure 3. Example SED fits. The left-hand panel shows the fit for one of our general population quasars, while the right-hand panel shows a fit for one of our BAL quasars. The photometric data are shown as blue triangles. The total fits are shown in solid black, while the two components of the fit are shown in the long dashed red (AGN) and the short dashed green (starburst) lines.

FIR emission from the AGN. We thus use the shorter wavelength data to constrain the properties of the AGN, and, having done so, then use the SPIRE data to constrain the properties of the starburst. Two example SED fits are given in Fig. 3; one for a classical quasar and one for a BAL quasar.

The AGN component of the fit includes both the direct emission and the reprocessed emission, that is, optical/ultraviolet light that is absorbed by the dust in the torus and reradiated in the infrared. We call the luminosity of the best-fitting AGN model the accretion luminosity, L_{acc}. We have assumed the smooth, continuous distribution of dust within the torus described in Fritz, Franceschini & Hatziminaoglou (2006) and Feltre et al. (2012). This set of models has been shown to accurately reproduce the SEDs of both obscured and unobscured AGN (e.g. Fritz et al. 2006; Hatziminaoglou et al. 2008, 2009; Gruppioni et al. 2016). We constrained the fit to a subset of 216 torus templates (out of the ∼3700 models in the full grid), selecting a representative set of parameters defined in Hatziminaoglou et al. (2008). This is done to minimize degeneracies among model parameters that we do not seek to constrain, without affecting the quality of the fits for the luminosities, given that there is a large overlap in SED shapes when varying the model parameters (for a description of the effect of each of the parameters on the SED, see Fritz et al. 2006).

The starburst component is modelled with a library of templates of six starburst galaxies: Arp220 (merger), M82 (disc/amorphous), M83 (SAB(s)c), NGC1482 (E/int), NGC4102 (Sb), and NGC7714 (Sc). The starburst templates span systems with low (e.g. M82 & M83, Nikola et al. 2012; Foyle et al. 2013) to high (e.g. Arp 220, Farrah et al. 2003; Rangwala et al. 2011) extinctions and a broad range in mid- to far-IR SED shapes, star-formation histories, and Hubble types. Thus, they plausibly span at least a substantial fraction of the properties of star-forming galaxies at $z > 0.5$ and have been used to model starbursts at all redshifts before (see e.g. Feltre et al. 2013). The luminosity of the starburst component, L_{SB}, is that of the best-fitting template scaled to the observed data points, integrated between 8 and 1000 µm. Finally, L_{SB} is then converted into an SFR using the original (i.e. assuming a Salpeter IMF) relation derived by Kennicutt (1998)

$$\frac{SFR}{M_\odot\ yr^{-1}} = 4.5 \times 10^{-44} \frac{L_{SB}}{erg\ s^{-1}}. \quad (1)$$
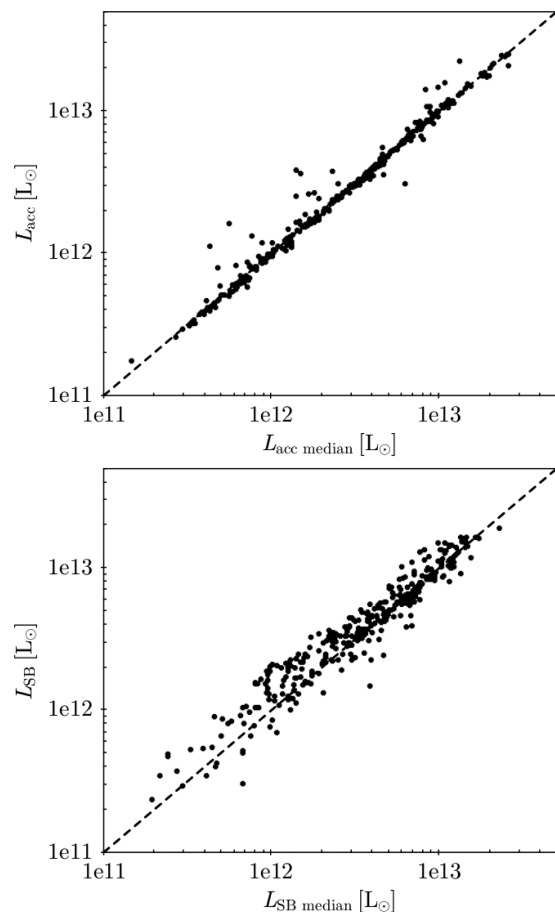

Figure 4. A comparison between the luminosities extracted from the best-fitting SEDs and from the median of their respective PDFs for L_{acc} (top) and L_{SB} (bottom). The agreement is excellent in both cases.

The L_{acc} and L_{SB} values derived from this approach have been shown to be robust (see Hatziminaoglou et al. 2008). To estimate the uncertainties on L_{acc} and L_{SB} specific to our set of templates, we calculate the median of the probability distribution function (PDF) of the values obtained using all combinations of models in the fit. Fig. 4 compares the best-fitting L_{acc} (top) and L_{SB} (bottom) with

the median of their respective PDFs. The root-mean-square deviation of the two sets of distributions are 7 per cent and 15 per cent, respectively. In other words, the best-fitting L_{acc} (L_{SB}) differs, on average by 7 (15) per cent from the median value of the PDF.

3.2 Black hole masses and Eddington ratios

We estimate BH masses (M_{BH}) from the FWHM of the C IV, Mg II or Hβ lines (e.g. Wandel, Peterson & Malkan 1999; Kaspi et al. 2000; McLure & Jarvis 2002), using:

$$\frac{M_{BH}}{M_{\odot}} = \alpha \left(\frac{\lambda L_{\lambda}}{10^{37} W} \right)^{\beta} \left(\frac{FWHM}{km\,s^{-1}} \right)^{2} \qquad (2)$$

with $\alpha = 4.6$, 5.2 and 8.2, $\beta = 0.53$, 0.62 and 0.50, and $\lambda = 1350$ Å, 3000 Å and 5100 Å for C IV, Mg II and Hβ, respectively, as described in Vestergaard & Peterson (2006) and Shen et al. (2011), the latter of which offers a recalibration of the Mg II formula initially described by McLure & Dunlop (2004). We then estimate Eddington ratio as $\lambda_{Edd} = L_{acc}/L_{Edd}$, where L_{Edd} is the Eddington luminosity, calculated as

$$\frac{L_{Edd}}{erg\,s^{-1}} = \frac{4\pi G m_{p} c}{\sigma_{T}} M_{BH} = 1.26 \times 10^{38} \frac{M_{BH}}{M_{\odot}} \qquad (3)$$

in which σ_{T} is the Thompson scattering cross-section for the electron, m_{p} is the mass of the proton, c is the speed of light and G the gravitational constant.

The uncertainties on the measurements of the FWHMs of C IV, Mg II, and Hβ are of the order of 10 per cent (Shen et al. 2011). The same authors discuss in detail the systematic errors on M_{BH} introduced by the use of the different emission lines. They show the offset between the estimates using Mg II and C IV to be negligible. For those objects in the redshift range such that both the C IV and Mg II lines are present in the spectra, we use the Mg II line as the BH mass tracer. There are no relevant emission line data available to compute the BH masses for eleven of our objects; we retain these objects in the sample but discard them from the relevant sections.

3.3 Complementarity with other studies

This paper complements and builds upon other works on the star-forming properties of quasar host galaxies. We here describe how it relates to the two most closely associated works, those of Ma & Yan (2015; hereafter MY15) and Harris et al. (2016; H16), respectively.

In many ways, the present work is an expansion of the work in MY15, who also study the star-forming properties of *Herschel*-selected SDSS quasars, using a sample of 354 quasars in all the HerMES DR2 catalogues, regardless of the depth of the fields, as well as the HerS and H-ATLAS (Eales et al. 2010) catalogues. Our sample, on the other hand, includes the HeLMS data, never previously been used in a study of this type, as well as HerS and the wider (and shallower) northern HerMES fields listed in Section 2.2. Moreover, while MY15 match SDSS positions to the positions in the HerMES, HerS and H-ATLAS public catalogues using a matching radius of 3 arcsec, we adopted a less conservative matching radius of 5 arcsec based on the simulations in Wang et al. (2014). From a visual inspection of all the sources, we find the resulting matches to be highly reliable. As a result of all the above, our *Herschel*/SDSS sample has 187 objects (about a third of its size) in common with the sample in MY15.

Our approach to extracting SFRs also differs to that used by MY15. MY15 considered the coldest dust component alone, by fitting a single-temperature modified blackbody to the SPIRE data. For
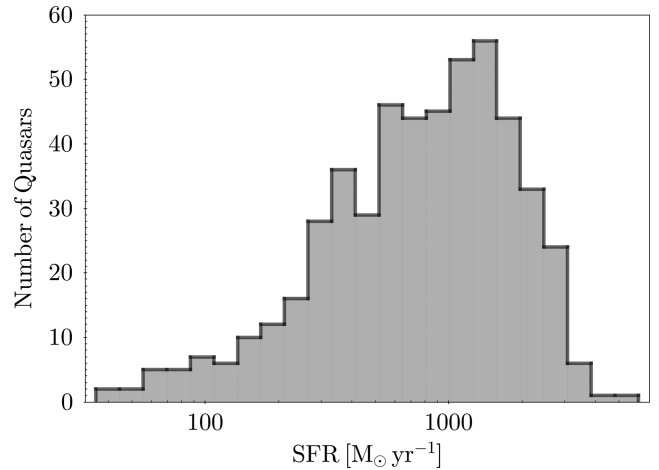

Figure 5. The SFR distribution for the *Herschel*/SDSS quasar sample. Our sample represents some of the most extreme starburst systems, as evidenced by the high inferred SFRs, which places them above the main sequence, for their respective redshifts, by over a dex on average.

testing purposes, a two-component SED fitting including an AGN and a starburst component was performed on a handful of objects with available PACS photometry. Conversely, in this work we constrain the AGN properties by focusing on the AGN-dominated part of the SED, using data in the near-IR (2MASS, UKIDSS or VHS photometry) and MIR (WISE), and by using a set of AGN models that have proved to accurately reproduce the optical-to-MIR quasar SED. Therefore, the key difference in the derived SFRs is that, in this work, the SFRs are measured on the full range 8–1000 μm, including the contribution to the MIR.

Turning to H16, our paper complements and extends this work. In H16, the authors also use *Herschel* data to study the star-forming properties of SDSS quasars. However, H16 focus on quasars in a narrower, systematically higher redshift range, $2 < z < 3$, and have a sample which is mostly individually *un*detected by *Herschel*. Hence their analysis relies on stacked observations rather than individual detections. At the same redshift, therefore, we study quasars with much higher SFRs on average.

4 RESULTS

4.1 Star formation rates

The distribution of the SFRs in our sample is shown in Fig. 5. The SFRs are extremely high, with a mean of 1000^{+1400}_{-600} M$_{\odot}$ yr^{-1}. This aligns well with those rates estimated for other individually FIR-detected populations, such as sub-millimetre galaxies (e.g. Chapman et al. 2010; Wardlow et al. 2011; Barger et al. 2014) and infrared-bright radio galaxies (e.g. Drouart et al. 2014), over a similar redshift range. The mean SFR is a factor ∼2 higher than that in MY15.[2] The difference is likely due to the fact that MY15 only considered SFRs measured from the coldest components, while our SFRs also include emission in the MIR.

Next, we examine the behaviour of the SFR as a function of L_{acc} (as defined in Section 3.1), M_{BH} and λ_{Edd}. To account for the fact

[2] MY15 quote 50 per cent of their objects exhibiting SFRs above 300 M$_{\odot}$ yr^{-1}, derived using Chabrier IMF. The value would be ∼510 M$_{\odot}$ yr^{-1} assuming a Salpeter IMF.

that this is a flux-limited sample, we split the sample into three redshift bins, $z < 1.0$, $1.0 \leq z < 2.0$ and $z \geq 2.0$. Each redshift bin is further split into L_{acc}, M_{BH}, or λ_{Edd} bins, and the average SFR is computed in each of these bins.

We find that the SFR increases by a factor of ~ 8 from the low ($z < 1.0$) to the high ($z \geq 2.0$) redshift bins for quasars of the same L_{acc}. In a given redshift interval, however, the SFR is consistent with being constant for increasing L_{acc} for all redshift bins. This is shown in the top panel of Fig. 6, where the average points are overplotted on the individual objects. The typical uncertainties on L_{acc} and L_{SB}, discussed in Section 3.1, are small relative to the size of the bins and have no effect on the results. The green line shows the relation described in H16 and will be discussed in Section 5. The bins in Fig. 6, however, are large, such that the apparent lack of a trend might be a result of degeneracies between redshift and luminosity. We tried a finer binning, with bins half the size of the ones presented here in terms of both redshift and luminosity, and found consistent results. We also found consistent results by examining SDSS DR7 and DR10 separately. The (lack of) trends are, therefore, not a bias as far as we can tell.

The middle panel of Fig. 6 plots SFR against M_{BH}. We again see that the SFR is constant with increasing M_{BH} inside a given redshift bin. Here there is no hint of a rise in SFR; while the uncertainties on the SFR and M_{BH} are significant, the data are entirely consistent with a flat relation. Finally, in the bottom panel of Fig. 6, we plot SFR against the Eddington ratios of the quasars. We again see no relation.

4.2 Broad absorption line quasars

A quasar is classified as BAL quasar if the equivalent width of at least one absorption line (usually C IV) exceeds 2000 km s^{-1} (Weymann et al. 1991). BAL quasars can be further split into three sub-populations. The most numerous of these is that of the high-ionization BAL (HiBAL) quasars. HiBAL quasars display absorption in Ly α λ1216 Å, N v λ1240 Å, Si IV λ1394 Å and C IV λ1549 Å. In addition to the absorption features found in HiBAL quasars' spectra, low-ionization BAL (LoBAL) quasars also display absorption features in such low-ionization ions as Al III λ1857 Å and Mg II λ2799 Å. The third class, FeLoBAL quasars, shares the same properties as LoBAL quasars with additional absorption features from excited levels of iron.

We select BAL quasars using the SDSS BAL_FLAG, which is set to 1 when C IV has an absorption feature, 2 when Mg II has one and 3 when both C IV and Mg II show absorption. Table 2 shows the number of BAL quasars in each of the three *Herschel* surveys with at least a 3σ detection at 250 μm. The *Herschel* detection rates of BAL quasars are around 5 per cent, identical to those of non-BAL quasars. Of the 59 BAL quasars detected in the three *Herschel* fields, 57 are HiBAL quasars and two are LoBAL quasars. As HiBAL and LoBAL quasars may be physically different (see e.g. Streblyanska et al. 2010), we restrict our analysis to the 57 HiBAL quasars.

We create two sub-samples from the sources in the rectangle in Fig. 1. The lower redshift cut ($z = 1.5$) corresponds approximately to the wavelength at which the C IV line shifts out of the SDSS bandpass, eliminating two of the BAL quasars, while the upper redshift cut ($z = 3.3$) is set where the quasar density drops significantly, and only leaves out one BAL quasar from the full set. The corresponding bright and faint absolute magnitude cuts are -28.5 and -24.3, respectively, leaving another three BAL quasars out. A total of 51 BAL and 208 non-BAL quasars reside in the defined area.
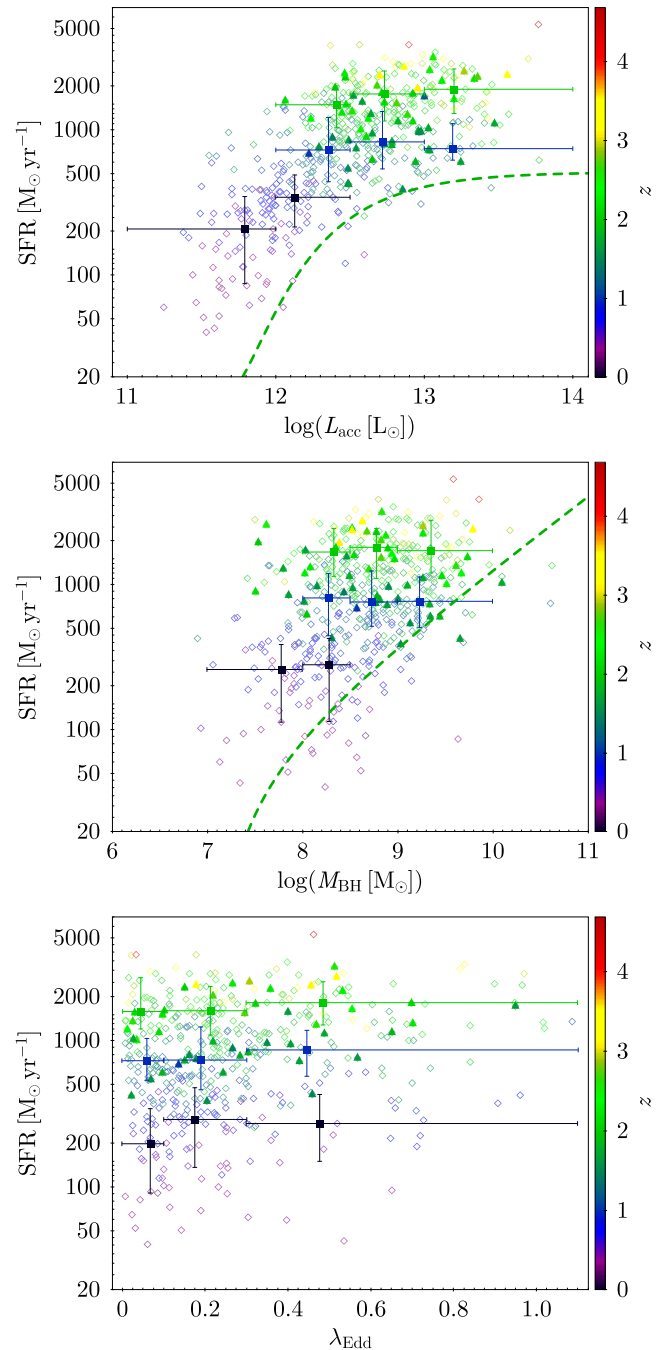

Figure 6. SFR versus L_{acc} (top panel), M_{BH} (middle panel) and λ_{Edd} (bottom panel), colour-coded by redshift. The three redshift bins are $z < 1.0$, $1.0 \leq z < 2.0$ and $z \geq 2.0$. SFRs increase with redshift, but do not correlate with any of the intrinsic quasar properties within the same redshift range. The green lines in the top and middle panels show the relations described in Harris et al. (2016) for quasars at $2 < z < 3$ with a factor $2 - 3$ lower SFRs than in our sample. The filled squares and associated error bars show the mean value in each bin. The diamonds and triangles show the results for the non-BAL and BAL sub-samples, respectively.

Looking at Fig. 6, there is no preferred location for the BAL quasars in any of the parameter spaces considered (the lack of BAL quasars with low SFR is due to the lower redshift cut). To further test if the behaviour of these BAL quasars is identical to that of the non-BAL quasars, we perform K–S tests to compare the L_{acc}, λ_{Edd} and SFR distributions of the two subsets. The BAL

Table 2. BAL detection statistics by *Herschel* field. The average *Herschel* detection rate of BAL quasars is about 5 per cent, the same as for non-BAL quasars, as shown in Table 1.

Field	SDSS BAL quasars	*Herschel*/SDSS BAL quasars
HerMES	92	7
HerS	344	20
HeLMS	666	32

quasars have indistinguishable L_{acc} and λ_{Edd} distribution from the non-BAL quasars, as indicated by the *p*-values from the K–S test (0.47 and 0.46, respectively). Lastly, their SFR distributions are also indistinguishable (*p*-value = 0.46). We thus find no evidence that the accretion rate, accretion efficiency or star forming properties of HiBAL quasars are different from those of classical quasars.

5 DISCUSSION AND CONCLUSIONS

The relationship between SFRs and AGN properties gives insights into the co-evolution of these activities. While we do not have stellar masses for our sample, their extremely high SFRs coupled with reasonable assumptions for quasar host stellar masses at this epoch mean they almost certainly lie above the 'main sequence' for star formation at their respective epochs. In the following, we consider the relationship between SFRs and both redshift and AGN properties. Finally, we discuss the implications for BAL quasars.

5.1 Evolution with redshift

We find that the SFRs of our sample increase by a factor of up to ~ 8 from $z < 1$ to $z \geq 2$. We do not see any evidence for a rise in SFRs with redshift beyond $z \sim 2$. This is consistent with observations of the global comoving SFR density, which increases by a factor of at least 10 over $0 < z < 1$ and peaks around $z = 2$ (e.g. Reddy et al. 2008; Magnelli et al. 2009; Karim et al. 2011; Wuyts et al. 2011; Béthermin et al. 2013; Burgarella et al. 2013; Wang et al. 2013; Chen et al. 2016). Thus, in terms of evolution over $0 \lesssim z \lesssim 3$, extremely luminous star formation events in quasar hosts appear to evolve, on average, in a manner consistent with the global star formation history as derived from the general galaxy population.

Our results are also consistent with those of MY15, who find that the fraction of IR-luminous quasars peaks at $z \sim 2$, and with H16, who find that SFRs in quasars do not change appreciably as a function of redshift over $2 < z < 3$ (but see also e.g. Netzer et al. 2016). They are also consistent with several previous studies of the evolution with redshift of star formation in AGN hosts (e.g. Serjeant & Hatziminaoglou 2009; Serjeant et al. 2010; Shao et al. 2010; Bonfield et al. 2011; Mullaney et al. 2012b). These previous studies mostly sample different parts of the z-SFR-L_{acc} parameter space for quasars to our study. For example, the sample in Mullaney et al. (2012b) spans a similar redshift range but has lower L_{acc} values and SFRs by $\gtrsim 2$ orders of magnitude, while the sample in H16 has comparable L_{acc} values, but lies at higher redshifts with a factor ~ 3 lower SFRs. The apparent consistency of our results with theirs on the evolution of SFRs with redshift in quasar hosts is thus remarkable. This consistency suggests that the physical processes that lead to star formation in AGN hosts, such as mergers or secular evolution, do so in a way that gives a similar evolution with redshift for star formation events spanning tens to thousands of $M_\odot$ per year and accretion luminosities $\gtrsim 10^{10}$ $L_\odot$. We caution however

that this does not account for selection effects between studies, and only applies to time-scales significantly longer than the AGN and starburst duty cycles.

5.2 Star formation and accretion luminosity

We first consider the relation between SFR and L_{acc}. The top panel of Fig. 6 is consistent with an approximately flat SFR $-L_{acc}$ relation, in all redshift bins. This is in agreement with some previous studies (e.g. Priddey et al. 2003; Shao et al. 2010; Dicken et al. 2012; Harrison et al. 2012; Mullaney et al. 2012b; Rosario et al. 2013; Banerji et al. 2015; MY15; Stanley et al. 2015), but not others (e.g. Netzer 2009; Hatziminaoglou et al. 2010; Imanishi et al. 2011; Rafferty et al. 2011; Mullaney et al. 2012a; Chen et al. 2013; Young et al. 2014; Delvecchio et al. 2015; Xu et al. 2015; Bian et al. 2016).

Several explanations for an observed lack of a relation between SFR and L_{acc} have been proposed. They fall, broadly, into four categories. First, the strength of the relation depends on redshift, with an observable relation only emerging at $z \gtrsim 2$ (Hatziminaoglou et al. 2010; Rovilos et al. 2012; Delvecchio et al. 2015; H16). This could arise due to, for example, a higher free gas fraction at higher redshifts. Secondly, AGN luminosities can vary substantially on time-scales of days to months. If AGN luminosities are measured using methods that are particularly sensitive to such variations, such as X-ray observations (Barr & Mushotzky 1986; Ulrich, Maraschi & Urry 1997; Grupe, Thomas & Beuermann 2001; Chitnis et al. 2009), then underlying trends could be masked (Gabor & Bournaud 2013; Volonteri et al. 2015). Thirdly, it is possible that at very high SFRs and/or L_{acc} values, we are sampling an intrinsically different quasar population, one in which e.g. a different trigger for star formation leads to a weaker or absent correlation between SFR and L_{acc}. Fourthly, at high SFRs or high L_{acc}, the properties of the starburst become decoupled from those of the AGN, plausibly because internal self-regulation processes become the dominant effect in regulating luminosities on time-scales comparable to or shorter than the AGN or starburst duty cycles.

The first possibility is, *on its own*, not plausible for our sample, as our sample spans a wide range in redshift and we do not see a significant correlation in any redshift bin. The second seems unlikely, since our sample is large and has AGN luminosities measured from optical, rather than X-ray data. We note however that there exists a conceptually similar possibility – that the duty cycles of starburst and AGN activity are sufficiently mismatched in duration that no correlation is observed between their luminosities. The available constraints on the duty cycle lengths of starburst and AGN phases are however not accurate enough for us to comment on this possibility. The third possibility also seems unlikely, since we found no differences between the *Herschel*/SDSS sample and the general SDSS quasar population in Section 2.1, though we cannot formally exclude it.

The fourth scenario, however, is plausible, since our sample harbours the highest SFRs seen in quasars, where self-regulation may be expected to be seen, if it occurs. Moreover, it is consistent with observations of systems with comparable SFRs at $z > 1$, i.e. sub-millimetre galaxies (SMGs, Barger et al. 2014), which exhibit a flattening in their SFRs at extremely high SFR values. An interesting corollary comes from the work of MY15, who find that star-forming regions in IR-luminous quasars do not increase in size at very high SFRs, but instead may increase in SFR *density*. An increase in SFR density could mean that starburst self-regulation becomes more effective, via e.g. approaching the Eddington limit for star formation, where winds from supernovae can expel free gas and thus stall

star formation (e.g. Murray, Quataert & Thompson 2005; Thompson, Quataert & Murray 2005; Diamond-Stanic et al. 2012). We thus propose that the flat relation between SFR and L_{acc} in our sample arises because self-regulation by the starburst becomes the dominant factor controlling the SFRs. We cannot, however, rule out a contribution from redshift-driven effects, or from mismatches in the lengths of duty cycles of starburst and AGN episodes.

The top panel of Fig. 6 also shows no downturn in SFRs at the highest L_{acc} values. This is, in principle, inconsistent with the idea that luminous AGN can quench star formation in their host galaxies (see also e.g. Villar-Martín et al. 2016). An alternative interpretation is however possible; *assuming that AGN feedback occurs*, this instead suggests that L_{acc} (as derived from rest-frame UV observations) is not a good proxy for the strength of AGN feedback. This is consistent with AGN feedback being a brief phase in the AGN duty cycle, signposted by properties other than AGN luminosity (e.g. Farrah et al. 2012).

5.3 Star formation, black hole masses, and Eddington ratios

The middle panel of Fig. 6 is consistent with there being no relation between SFR and M_{BH}. This lack of a correlation is, in some senses, surprising. For example, it has been suggested that SFRs should scale with M_{BH} in quasars since SFRs should scale with the total available free gas mass or its large-scale distribution (Cen 2015), and both the free gas mass and M_{BH} should scale with the total baryon density. Thus, on $\gtrsim 100$ Myr time-scales, SFRs and M_{BH} in quasars may be expected to correlate since a larger free baryon reservoir would favour both higher current SFRs and higher L_{acc} *in the past*. We, however, do not see such a correlation.

A plausible explanation comes from considering our results in context with those of H16, who found that SFRs in quasars at $2 < z < 3$ do correlate with M_{BH} (and L_{acc}), but only up to an SFR of $\sim 600 \, M_{\odot} \, yr^{-1}$. Above this SFR, they find no correlation. Our SFRs are mostly higher than those in H16 and are measured individually, rather than stacked as in H16, so it is interesting to compare their results to ours. In the top and middle panels of Fig. 6, we plot the relations that H16 derive between SFR and L_{acc} and M_{BH}, respectively. For the SFR–L_{acc} plot our results are, given the sizes of the error bars on the average points in each redshift bin, consistent with the H16 relation. For the SFR–M_{BH} plot the consistency is weaker, but fig. 17 of H16 shows, plausibly, a flattening in the SFR–M_{BH} relation at about $600 \, M_{\odot} \, yr^{-1}$ as well. Overall therefore, we argue that our results and those in H16 are both consistent with the idea that SFRs in quasars correlate with L_{acc} and M_{BH}, but only up to an SFR when internal 'self-regulation' by the starburst becomes important.

The bottom panel of Fig. 6 is consistent with there being no relation between SFR and λ_{Edd}, at any redshift. This result is also in line with those in H16, who also find no evidence for an SFR $- \lambda_{Edd}$ relation, at any SFR (modulo possible enhanced SFRs at low λ_{Edd} values). Overall, this is consistent with there being no relation between SFRs in quasars and how efficiently the black hole is accreting, at *any* SFR. It is also consistent with the suggestion that λ_{Edd} values in quasars do not depend strongly on redshift, at least at $z \gtrsim 0.5$ (e.g. Shankar, Weinberg & Miralda-Escudé 2013; Caplar, Lilly & Trakhtenbrot 2015; see also Fine et al. 2006; Bluck et al. 2011; Lusso et al. 2012).

5.4 Star formation in broad absorption line quasars

We find that there is no difference in the SFR, L_{acc}, M_{BH} and λ_{Edd} distributions between the HiBAL and non-BAL quasars in our sample; all are consistent with being drawn from the same parent population. A minor caveat to this result is that our sample may be incomplete for HiBALs at very high redshifts (Section 2.1), an effect that we cannot account for using available data; we think it unlikely that this incompleteness could be a significant factor leading to the lack of differences between BAL and non-BAL quasars that we observe.

This result aligns with previous studies, which find no differences between HiBAL and classical quasars, at any redshift (Priddey et al. 2003, 2007; Gallagher et al. 2007; Pu 2015; H16). In particular, it is consistent with the study of Cao Orjales et al. (2012), who also use *Herschel*-SPIRE data to compare the properties of BAL versus non-BAL quasars, from the H-ATLAS survey, and find no differences between the two populations. The two studies, however, sample different regimes in SFR; our study examines quasars with typical SFRs of $\sim 1000 \, M_{\odot} \, yr^{-1}$, whereas the typical SFRs of the quasars in Cao Orjales et al. (2012) are $\sim 240 \, M_{\odot} \, yr^{-1}$. The combined results suggest that BALs are not seen preferentially in certain L_{acc} or M_{BH} regimes, and not over specific ranges in SFR, even for those quasars harbouring the most luminous star formation events seen in any quasar at any redshift.

It has been argued that BAL quasars may be a promising quasar population within which to look for evidence of AGN feedback, since the BAL winds provide a natural mechanism to couple momentum from accretion-disc winds to ISM gas. The lack of any differences between the HiBALs and the non-BALs in our sample however argues that HiBAL quasars are, as a population, not sites for AGN feedback, unless the AGN feedback phase is much shorter than the lifetime of the BAL winds. Instead, our results are consistent with HiBAL quasars being normal quasars observed along a particular line of sight, with the outflows in HiBAL quasars not having any measurable effect on the star formation in their hosts (see also e.g. Violino et al. 2016).

described in Oliver et al. (2012). The HerMES data presented in this paper are available through the *Herschel* Database in Marseille (http://hedam.lam.fr/HerMES/). AF acknowledges support from the ERC via an Advanced Grant under grant agreement no. 321323 NEOGAL. This work makes extensive use of TOPCAT (Taylor 2005).

REFERENCES

Alaghband-Zadeh S., Banerji M., Hewett P. C., McMahon R. G., 2016, MNRAS, 459, 999
Alexander D. M., Bauer F. E., Chapman S. C., Smail I., Blain A. W., Brandt W. N., Ivison R. J., 2005, ApJ, 632, 736
Banerji M. et al., 2015, MNRAS, 454, 419
Barger A. J. et al., 2014, ApJ, 784, 9
Barr P., Mushotzky R. F., 1986, Nature, 320, 421
Béthermin M., Wang L., Doré O., Lagache G., Sargent M., Daddi E., Cousin M., Aussel H., 2013, A&A, 557, A66
Bian W.-H., He Z.-C., Green R., Shi Y., Ge X., Liu W.-S., 2016, MNRAS, 456, 4081
Bluck A. F. L., Conselice C. J., Almaini O., Laird E. S., Nandra K., Grützbauch R., 2011, MNRAS, 410, 1174
Bonfield D. G. et al., 2011, MNRAS, 416, 13
Booth C. M., Schaye J., 2009, MNRAS, 398, 53
Bower R. G., Benson A. J., Malbon R., Helly J. C., Frenk C. S., Baugh C. M., Cole S., Lacey C. G., 2006, MNRAS, 370, 645
Bridge C. R. et al., 2013, ApJ, 769, 91
Burgarella D. et al., 2013, A&A, 554, A70
Cao Orjales J. M. et al., 2012, MNRAS, 427, 1209
Caplar N., Lilly S. J., Trakhtenbrot B., 2015, ApJ, 811, 148
Carilli C. L. et al., 2001, ApJ, 555, 625
Cen R., 2015, ApJ, 805, L9
Chapman S. C. et al., 2010, MNRAS, 409, L13
Chartas G., Brandt W. N., Gallagher S. C., 2003, ApJ, 595, 85
Chen C.-T. J. et al., 2013, ApJ, 773, 3
Chen C.-C. et al., 2016, ApJ, 820, 82
Chitnis V. R., Pendharkar J. K., Bose D., Agrawal V. K., Rao A. R., Misra R., 2009, ApJ, 698, 1207
Clarke C. L., 2016, The distant, dusty Universe: finding star-forming galaxies with the Herschel Space Observatory. PhD thesis, Univ. Sussex
Croton D. et al., 2006, MNRAS, 365, 11
de Kool M., Becker R. H., Arav N., Gregg M. D., White R. L., 2002, ApJ, 570, 514
Delvecchio I. et al., 2015, MNRAS, 449, 373
Diamond-Stanic A. M., Moustakas J., Tremonti C. A., Coil A. L., Hickox R. C., Robaina A. R., Rudnick G. H., Sell P. H., 2012, ApJ, 755, L26
Dicken D. et al., 2012, ApJ, 745, 172
Diolaiti E., Bendinelli O., Bonaccini D., Close L. M., Currie D. G., Parmeggiani G., 2000, A&AS, 147, 335
Drouart G. et al., 2014, A&A, 566, A53
Eales S. et al., 2010 PASP, 122, 499
Efstathiou A. et al., 2014, MNRAS, 437, L16
Elbaz D. et al., 2011, A&A, 533, A119
Elvis M., 2000, ApJ, 545, 63
Fabian A. C., 2012, ARA&A, 50, 455
Farrah D., Serjeant S., Efstathiou A., Rowan-Robinson M., Verma A., 2002, MNRAS, 335, 1163
Farrah D., Afonso J., Efstathiou A., Rowan-Robinson M., Fox M., Clements D., 2003, MNRAS, 343, 585
Farrah D. et al., 2009, ApJ, 700, 395
Farrah D. et al., 2012, ApJ, 745, 178
Feltre A., Hatziminaoglou E., Fritz J., Franceschini A., 2012, MNRAS, 426, 120
Feltre A. et al., 2013, MNRAS, 434, 2426
Ferrarese L., Merritt D., 2000, ApJ, 539, L9
Feruglio C., Maiolino R., Piconcelli E., Menci N., Aussel H., Lamastra A., Fiore F., 2010, A&A, 518, 155

Fine S. et al., 2006, MNRAS, 373, 613
Foyle K. et al., 2013, MNRAS, 432, 2182
Fritz J., Franceschini A., Hatziminaoglou E., 2006, MNRAS, 366, 767
Gabor J. M., Bournaud F., 2013, MNRAS, 434, 606
Gallagher S. C., Hines D. C., Blaylock M., Priddey R. S., Brandt W. N., Egami E. E., 2007, ApJ, 665, 157
Genzel R. et al., 1998, ApJ, 498, 579
Griffin M. J. et al., 2010, A&A, 518, L3
Grupe D., Thomas H.-C., Beuermann K., 2001, A&A, 367, 470
Gruppioni C. et al., 2016, MNRAS, 458, 4297
Häring N., Rix H.-W., 2004, ApJ, 604, L89
Harris K. A. et al., 2016, MNRAS, 457, 4179 (H16)
Harrison C. M. et al., 2012, ApJ, 760, L15
Harrison C. M., Alexander D. M., Mullaney J. R., Swinbank A. M., 2014, MNRAS, 441, 3306
Hatziminaoglou E. et al., 2005 AJ, 129, 1198
Hatziminaoglou E. et al., 2008 MNRAS, 386, 1252
Hatziminaoglou E., Fritz J., Jarrett T. H., 2009, MNRAS, 399, 1206
Hatziminaoglou E. et al., 2010, A&A, 518, L33
Hernán-Caballero A. et al., 2009, MNRAS, 395, 1695
Hewett P. C., Foltz C. B., 2003, AJ, 125, 1784
Imanishi M., Ichikawa K., Takeuchi T., Kawakatu N., Oi N., Imase K., 2011, PASJ, 63, 447
Karim A. et al., 2011, ApJ, 730, 61
Kaspi S., Smith P. S., Netzer H., Maoz D., Jannuzi B. T., Giveon U., 2000, ApJ, 533, 631
Kennicutt R. C., Jr, 1998, ARA&A, 36, 189
LaMassa S. M., Heckman T. M., Ptak A., Urry C. M., 2013, ApJ, 756, L33
Lawrence A. et al., 2007, MNRAS, 379, 1599
Lusso E. et al., 2012, MNRAS, 425, 623
Lynds C. R., 1967, ApJ, 147, 396
Ma Z., Yan H., 2015, ApJ, 811, 58 (MY15)
Magdis G. E. et al., 2014, ApJ, 796, 63
Magnelli B., Elbaz D., Chary R. R., Dickinson M., Le Borgne D., Frayer D. T., Willmer C. N. A., 2009, A&A, 496, 57
Magorrian J. et al., 1998, AJ, 115, 2285
Mainieri V. et al., 2011, A&A, 535 80
Martínez-Sansigre A., Rawlings S., Lacy M., Fadda D., Marleau F. R., Simpson C., Willott C. J., Jarvis M. J., 2005, Nature, 436, 666
McLure R. J., Dunlop J. S., 2004, MNRAS, 352, 1390
McLure R. J., Jarvis M. J., 2002, MNRAS, 337, 109
McMahon R. G. et al., 2013, The Messenger, 154, 35
Mullaney J. R. et al., 2012a, ApJ, 753, L30
Mullaney J. R. et al., 2012b, MNRAS, 419, 95
Murray N., Quataert E., Thompson T. A., 2005, ApJ, 618, 569
Netzer H., 2009, MNRAS, 399, 1907
Netzer H., Lani C., Nordon R., Trakhtenbrot B., Lira P., Shemmer O., 2016, ApJ, 819, 123
Nikola T. et al., 2012, ApJ, 749, L19
Oliver S. et al., 2012, MNRAS, 424, 1614
Omont A., Cox P., Bertoldi F., McMahon R. G., Carilli C., Isaak K. G., 2001, A&A, 374, 371
Page M. J. et al., 2012, Nature, 485, 213
Pâris I. et al., 2014, A&A, 563, A54
Perna M. et al., 2015, A&A, 574, 82
Pilbratt G. L. et al., 2010, A&A, 518, L1
Priddey R. S., Isaak K. G., McMahon R. G., Omont A., 2003, MNRAS, 339, 1183
Priddey R. S., Gallagher S. C., Isaak K. G., Sharp R. G., McMahon R. G., Butner H. M., 2007, MNRAS, 374, 867
Pu X., 2015, Ap&SS, 357, 3
Rafferty D. A., Brandt W. N., Alexander D. M., Xue Y. Q., Bauer F. E., Lehmer B. D., Luo B., Papovich C., 2011, ApJ, 742, 3
Rangwala N. et al., 2011, ApJ, 743, 94
Reddy N. A., Steidel C. C., Pettini M., Adelberger K. L., Shapley A. E., Erb D. K., Dickinson M., 2008, ApJS, 175, 48
Richards G. T. et al., 2002, AJ, 123, 2945
Rodighiero G. et al., 2011, ApJ, 739, L40

Rosario D. J. et al., 2013, A&A, 560, A72
Roseboom I. G. et al., 2010, MNRAS, 409, 48
Roseboom I. G. et al., 2012, MNRAS, 419, 2758
Rosenberg M. J. F. et al., 2015, ApJ, 801, 72
Ross N. P. et al., 2012, ApJS, 199, 3
Rovilos E. et al., 2012, A&A, 546, A58
Schneider D. P. et al., 2010, AJ, 139, 2360
Schreiber C. et al., 2015, A&A, 575, A74
Serjeant S., Hatziminaoglou E., 2009, MNRAS, 397, 265
Serjeant S. et al., 2010, A&A, 518, L7
Shankar F., Weinberg D. H., Miralda-Escudé J., 2013, MNRAS, 428, 421
Shao L. et al., 2010, A&A, 518, L26
Shen Y. et al., 2011, ApJS, 194, 45
Shi Y., Rieke G. H., Ogle P., Jiang L., Diamond-Stanic A. L., 2009, ApJ, 703, 1107
Skrutskie M. F. et al., 2006, AJ, 131, 1163
Smith A. J. et al., 2012, MNRAS, 419, 377
Spoon H. W. W. et al., 2013, ApJ, 775, 127
Stanley F., Harrison C. M., Alexander D. M., Swinbank A. M., Aird J. A., Del Moro A., Hickox R. C., Mullaney J. R., 2015, MNRAS, 453, 591
Streblyanska A., Barcons X., Carrera F. J., Gil-Merino R., 2010, A&A, 515, A2
Taylor M. B., 2005, in Shopbell P., Britton M., Ebert R., eds, ASP Conf. Ser. Vol. 347, Astronomical Data Analysis Software and Systems XIV. Astron. Soc. Pac., San Francisco, p. 29
Thompson T. A., Quataert E., Murray N., 2005, ApJ, 630, 167
Tremaine S. et al., 2002, ApJ, 574, 740

Turnshek D. A., 1984, ApJ, 280, 51
Ulrich M.-H., Maraschi L., Urry C. M., 1997, ARA&A, 35, 445
Vestergaard M., Peterson B. M., 2006, ApJ, 641, 689
Viero M. P. et al., 2014, ApJS, 210, 22
Villar-Martín M., Arribas S., Emonts B., Humphrey A., Tadhunter C., Bessiere P., Cabrera Lavers A., Ramos Almeida C., 2016, MNRAS, 460, 130
Violino G. et al., 2016, MNRAS, 457, 1371
Volonteri M., Capelo P. R., Netzer H., Bellovary J., Dotti M., Governato F., 2015, MNRAS, 449, 1470
Wandel A., Peterson B. M., Malkan M. A., 1999, ApJ, 526, 579
Wang L. et al., 2013, MNRAS, 431, 648
Wang L. et al., 2014, MNRAS, 444, 2870
Wang L. et al., 2015, MNRAS, 449, 4476
Wardlow J. L. I. et al., 2011, MNRAS, 415, 1479
Weymann R. J., Morris S. L., Foltz C. B., Hewett P. C., 1991, ApJ, 373, 23
White M. et al., 2012, MNRAS, 424, 933
Wright E. L. et al., 2010, AJ, 140, 1868
Wuyts S. et al., 2011, ApJ, 742, 96
Xu L., Rieke G. H., Egami E., Haines C. P., Pereira M. J., Smith G. P., 2015, ApJ, 808, 159
Young J. E., Eracleous M., Shemmer O., Netzer H., Gronwall C., Lutz D., Ciardullo R., Sturm E., 2014, MNRAS, 438, 217

This paper has been typeset from a TEX/LATEX file prepared by the author.